

Effect of Coriolis acceleration on the span-wise vorticity field over a wind-turbine airfoil

Pedro T. Rodrigues*, Elmer M. Gennaro[†], and Daniel S. Souza[‡]

São Paulo State University (UNESP), Campus of São João da Boa Vista, São João da Boa Vista, SP, 13876-750

The rotation is known to reduce the volume of the region of separated flow on inboard sections of horizontal-axis wind turbine blades. This reduction is frequently attributed to centrifugal pumping. However, recent investigations on the rotational stabilization of leading-edge vortex suggest that the radial transport of vorticity may not be the dominant mechanism limiting the vortex circulation on inboard sections of insect wings. For such low-Reynolds number, the effect of the tangential component of the Coriolis force destroys radial vorticity, limiting the growth of the leading-edge vortex and stabilizing it. However, to the best knowledge of the authors, the contribution of such a phenomenon to the rotational augmentation observed in wind turbines has not been assessed. We employed quasi-3D simulations to investigate the role of the Coriolis acceleration to the balance of span-wise vorticity within the region of separated flow on the upper surface of wind-turbine-blade sections at high angles of attack. The destruction rate of radial vorticity due to Coriolis acceleration was most significant in the free shear layer on the upper boundary of the separated-flow region. Moreover, it is shown that its integrated effect may be comparable to the rate of vorticity flowing in the recirculation region from the boundary layer. Therefore, the mechanism may be relevant to rotational augmentation observed in inboard sections of wind-turbines blades.

I. Introduction

Inboard sections of rotating wings have an improved capability to generate lift in comparison to the corresponding airfoil at linear motion in analogous conditions (local angle of attack and Reynolds number) [1, 2]. One of the mechanisms responsible for the rotational augmentation is the enhanced resistance of the boundary layer to separation due to the chord-wise component of the Coriolis acceleration. However, at high angles of attack, for which boundary-layer separation occurs even at sections of rotating blades, it is commonly observed that the size of the recirculation region is significantly reduced due to rotation. A reduction in suction surface pressure accompanies this effect compared to a two-dimensional moving airfoil.

Analyses of the three-dimensional boundary-layer equations considering the effect of rotation by Dumitrescu et al. [3] suggested the occurrence of a span-wise standing vortex on the blade suction surface. According to their results the vortex emanates from sections where the chord to radius ratio lies between 0.5 and 1.0, depending on the imposed pressure gradient. Analysing unsteady pressure measurements from the suction side of inboard blade sections of a horizontal-axis wind turbine (HAWT), Schreck et al. [4] observed that a high increase of the lift coefficient, in comparison to 2D flow, is associated with the presence of a stationary vortex over the blade surface. Similar conclusions were drawn from the 3D simulations by Mauro et al. [5] of a small-scale HAWT. Comparing the flow field over an inboard section of HAWT blade with the 2D flow field for the same angle of attack (AoA), Bangsa et al. [6] showed a significant reduction of the volume of the recirculating region for the blade section. They attributed this volume reduction to centrifugal pumping and argued that it represents a weakening of the decambering effect, explaining the lift augmentation.

Due to rotation, the blades of rotary wings are subjected to a radial gradient of the dynamic pressure of the incoming flow. This gradient often results in a static-pressure radial gradient within the boundary layer, which tends to accelerate the secondary flow towards the blade tip [7]. Moreover, the centrifugal acceleration perceived by an observer attached to the blade increases with distance to the axis of rotation [8, 9]. This effect also accelerates the flow towards the tip and is commonly referred to as centrifugal pumping.

*Undergraduate student, Aeronautical Engineering, Av. Profa. Isette Correa Fontão, 505 - Jardim das Flores, São João da Boa Vista, Brazil.

[†]Assistant Professor, Aeronautical Engineering, Av. Profa. Isette Correa Fontão, 505 - Jardim das Flores, São João da Boa Vista, Brazil.

[‡]Assistant Professor, Aeronautical Engineering, Av. Profa. Isette Correa Fontão, 505 - Jardim das Flores, São João da Boa Vista, Brazil.

The secondary flow driven by the radial gradients of pressure and centrifugal force is frequently pointed to the mechanism responsible for stabilizing the leading-edge vortex (LEV) on insect flights [7]. Similar to what is observed in delta wings, the radial flow acceleration drains span-wise vorticity out of the boundary layer over inboard sections towards the blade tip, limiting the growth of the LEV and preventing its breakdown. However, recent investigations suggested that other effects may be relevant for stabilizing the LEV on insect wings [10–12].

Based on stereoscopic particle image velocimetry, Wojcik and Buchholtz [10] computed the radial transport of span-wise vorticity at different sections of a rotating rectangular flat plate at a geometric AoA of 35° . They analyzed the vorticity budget in the LEV and showed that the radial transport of vorticity was not sufficient to restrict the LEV circulation for a Reynolds of 4000 based on the tip speed. On the other hand, 3D simulations by Werner et al. [12] showed that a tilt of the planetary vorticity in regions of high absolute values of span-wise vorticity may act locally as a source of opposite sign vorticity. According to their results, at conditions corresponding to fruit- and house-fly flight, this radial planetary vorticity tilting may limit the amount of vorticity ingested by the LEV, thus contributing to its stabilization.

We investigated the relevance of the term associated with the radial planetary vorticity tilting to the balance of the radial vorticity within the region of separated flow on the upper surface of a HAWT section using numerical simulations. A quasi-3D model was employed, based on the one proposed by Chaviaropoulos and Hansen [13], and three different angles of attack were considered. Each considered AoA was simulated in a two-dimensional flow and at a condition corresponding to a section of HAWT.

II. Quasi-3D simulations

Figure 1 schematically represents the local flow on a wind-turbine section at a distance r from the axis of rotation. A quasi-3D model, similar to the one proposed by Chaviaropoulos and Hansen [13], was implemented to identify the rotational effects on different blade sections. The governing equations of the model were derived from the conservative form of the three-dimensional incompressible Navier-Stokes equation written in cylindrical coordinates for a frame of reference which rotates with the blade at a constant angular speed Ω . This set of equations was averaged along a strip in the radial direction. Henceforward, a condition of zero radial gradient of the total pressure was assumed and the average of the radial derivatives of the velocity components was neglected. Moreover, it was assumed that mean values of products could be approximated with products of mean values. We further neglected terms associated to the curvature, except terms proportional to U_∞/r , since the magnitude of the free-stream velocity U_∞ scales with r .

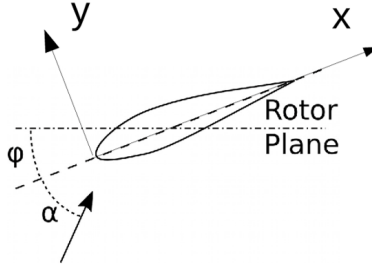


Fig. 1 Schematic view of the flow on the section of a horizontal-axis wind turbine blade.

With the assumptions mentioned above, the governing equations simplified to

$$\nabla_{2D} \cdot \mathbf{V} = 0, \quad (1)$$

$$\nabla_{2D} \cdot (\rho u \mathbf{V} - \mu \nabla_{2D} u) + \frac{\partial p}{\partial x} = 2\rho w \left(\Omega - \frac{u \cos \varphi}{r} + \frac{v \sin \varphi}{r} \right) \cos \varphi, \quad (2)$$

$$\nabla_{2D} \cdot (\rho v \mathbf{V} - \mu \nabla_{2D} v) + \frac{\partial p}{\partial y} = -2\rho w \left(\Omega - \frac{u \cos \varphi}{r} + \frac{v \sin \varphi}{r} \right) \sin \varphi, \quad (3)$$

$$\nabla_{2D} \cdot (\rho w \mathbf{V} - \mu \nabla_{2D} w) = \frac{\rho}{r} [2(u \cos \varphi - v \sin \varphi - \Omega r)^2 - w^2], \quad (4)$$

where $\mathbf{V} = (u, v)$ is the sectional velocity, u and v are the local chord-wise and normal-to-chord velocity components, respectively, w is the span-wise velocity component, r is the radial coordinate, $\nabla_{2D} \equiv (\partial/\partial x, \partial/\partial y)$, x and y are the local Cartesian coordinates, μ e ρ are the dynamic viscosity and density, respectively, p is the static pressure, U_∞ is the local far-field velocity magnitude, Ω is the angular velocity, α is the local angle of attack and c is the chord. The local pitch angle φ is related to the Rossby number, $Ro = U_\infty/(c\Omega)$, and to the chord-to-radius ratio through $\varphi = \cos^{-1} [1/(c/r Ro)] - \alpha$.

The numerical results were obtained from pressure-based incompressible Reynolds averaged Navier-Stokes (RANS) simulations performed with the finite volume software ANSYS Fluent[®]. The SIMPLE algorithm was employed for the pressure-velocity coupling. The convective terms were discretized with a second-order linear-upwind scheme and the diffusion terms with a second-order central-differences linear scheme. The flow was assumed to be fully turbulent and the effect of turbulence was modeled with the SST $k-\omega$ model [14]. In the outer domain boundary, the velocity was prescribed to result in the intended Reynolds number and angle of attack. There, the radial velocity component was set to zero.

The chosen mesh was a structured O -grid type. The dimension of the domain and mesh refinement were determined by means of convergence studies. The employed grid (Fig. 2) was sufficient for the simulations discussed here to keep the y^+ on the airfoil surface below 3. We considered the flow over the 21% thick S809 airfoil, which was designed by Somers [15] for application in wind turbines.

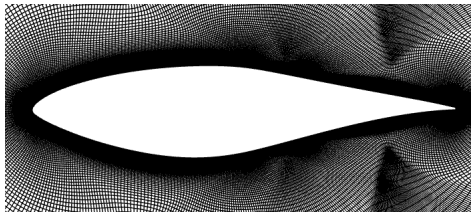


Fig. 2 Structured mesh in detail around S809 airfoil.

III. Results and Discussions

A. Solution sensitiveness to grid refinement

The sensitiveness of the results to the grid refinement was assessed through a series of simulations for conditions without rotational effects. For this series of computations, a Reynolds number of 1 million was adopted, based on the chord and free-stream velocity. Figure 3 shows predicted aerodynamic coefficients for different mesh refinement, considering different numbers of points along the airfoil surface and wind-tunnel measurements [15]. It is observed that the grid with 500 points on the airfoil surface was sufficient to achieve a reasonable level of convergence. Moreover, the predictions showed a good correlation with measurements by Somers [15].

B. Rotational effects on the flow field

To assess the accuracy of the simulation model considering rotation, we compared aerodynamic loading distribution for the case $\alpha = 15^\circ$ with the results obtained by Chaviaropoulos and Hansen [13]. In the simulations, Chaviaropoulos and Hansen [13] considered the NACA63-415 airfoil and maintained a fixed relationship between Ro and c/r given by $Ro = [c/r \cos(\alpha)]^{-1}$ considering $Re = 2 \times 10^6$. Figure 4 shows the distribution of the pressure coefficient along the chord of the airfoil S809 for the same values of c/r ratio and Rossby numbers, however considering $Re = 10^6$. Although not shown here, preliminary simulations at $Re = 10^6$ and $Re = 2 \times 10^6$ at a higher angle of attack showed no significant effect of the Reynolds number at this range.

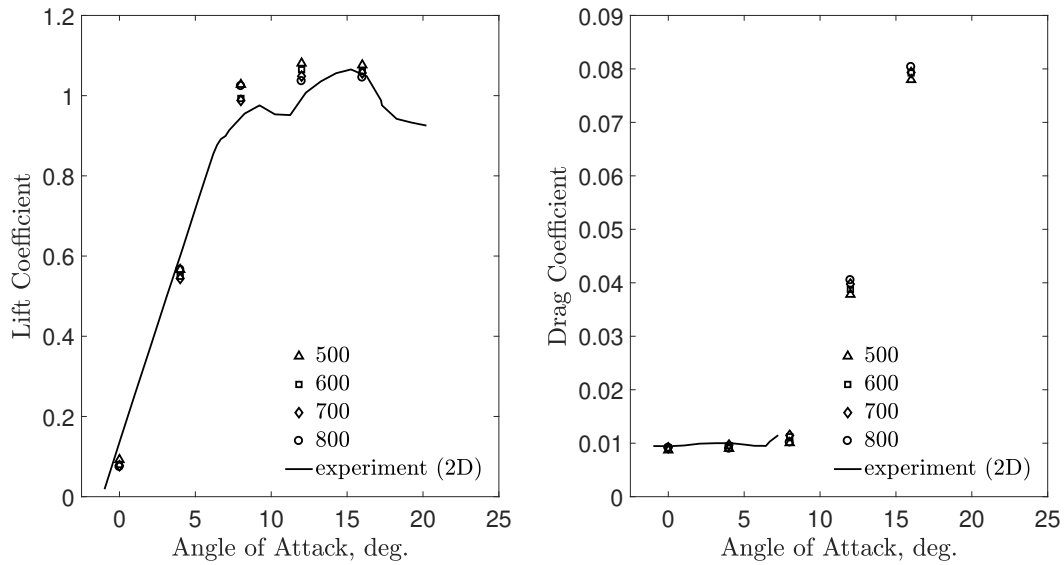


Fig. 3 Lift (left-hand side) and drag (right-hand side) coefficients. Computations for different meshes (markers) and experimental data from Somers [15].

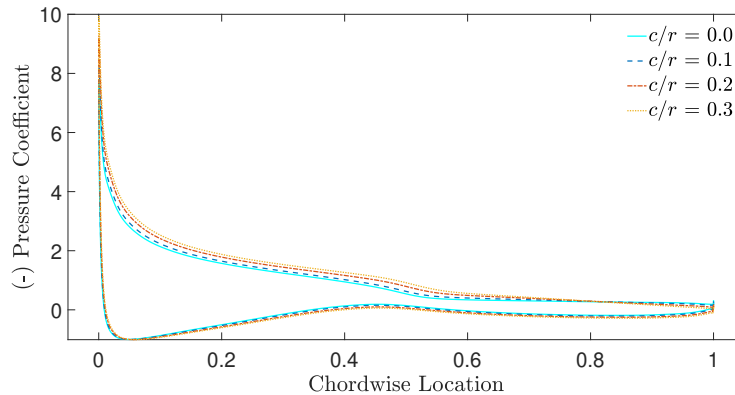


Fig. 4 Pressure coefficient distribution for S809 airfoil considering $Re = 10^6$, $\alpha = 15^\circ$ and zero twist.

From Fig. 4, it is observed that the curve obtained for the distribution of the pressure coefficient is similar to that obtained by Chaviaropoulos and Hansen [13, p. 335, Fig. 6(a)] along the chord of the NACA63-415 airfoil. This result is valuable, since in the quasi-3D modeling carried out in the present work, the effects of curvature in viscous forces and the continuity equation were neglected and even so similar results were obtained, indicating that these terms might have limited relevance under these conditions. It is also noted that as c/r increases there is an increase in the loading and, consequently, in the sectional lift. This effect can be attributed to the occurrence of mechanisms arising from non-inertial forces acting on the sections considered and which are consistent with the increase in lift due to rotation.

Simulations were run for AoA of 10° , 15° and 27° . For each angle of attack, flows without and with rotation were considered. The values of c/r and Ro of the cases with rotation were chosen to be representative of sections of a small-scale wind turbine.

Table 1 shows the set of selected cases and the predicted lift and drag coefficients. For the three considered angles of attack, the lift increased with rotation. Nevertheless, the effect of rotation on the drag was not unique, as it caused a drag reduction for $\alpha = 10^\circ$ and increased the drag for the other two simulated AoA. This variable effect of rotation on the

section drag is commonly reported in the literature and it is sometimes suggested that it depends on the airfoil geometry [16]. However, three-dimensional, span-wise periodic simulations of the flow over the S809 airfoil revealed the same AoA dependence of the rotational effect on drag [17].

Table 1 Set of chosen cases.

α	c/r	Ro	C_l	C_d
10°	0.0000	∞	1.03	0.0245
10°	0.0625	16	1.05	0.0236
15°	0.0000	∞	1.20	0.0555
15°	0.4500	3.0	1.50	0.0571
27°	0.0000	∞	1.15	0.6705
27°	0.3000	3.5	1.72	0.7770

Figure 5 shows the pressure coefficient distributions on the surface of the S809 airfoil considering experimental and simulation data for AoA close to 10° and 27°, according to the availability of data in the literature [15, 18]. In general, the qualitative effect of rotation was captured by the simulations. However, the load was slightly overpredicted, except for the condition with $Ro = 3.5$. For this case, the measured time-averaged pressure coefficient curve on the upper surface had a rounded shape while the simulation predicted an almost linear pressure increase, expected in trailing-edge separation on rotating sections [19]. This difference might be attributed to three-dimensional effects of the flow in this region that were not captured by the quasi-3D model used or to the different c/r and AoA of the compared conditions.

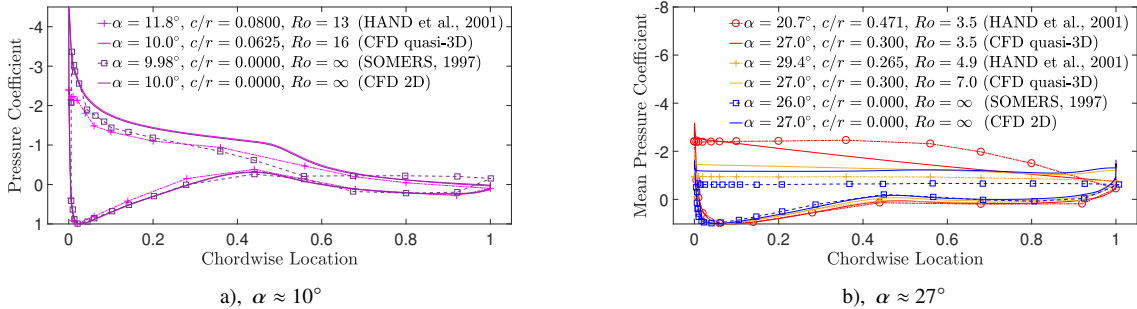


Fig. 5 (a) Pressure coefficient distribution for $\alpha \approx 10^\circ$ and (b) mean pressure coefficient distribution for $\alpha \approx 27^\circ$ (right-hand side).

Figure 6 shows the pressure coefficient distribution on the airfoil surface, based only on the simulations, together with the predicted chordwise location of the upper-surface boundary-layer separation point. The separation point was considered as the locus where the skin frictional coefficient equals zero. It is seen that the effect of rotation on the pressure distribution was stronger for the higher angles of attack. However, for the three considered AoA, the separation point shifted downstream. It is also observed that, in the region of separated flow, the pressure distribution assumed a triangular shape in the presence of rotational effects, while it is approximately uniform for the two-dimensional cases. The result agrees with observations highlighted by Souza and Gennaro [17] and Sicot et al. [19]. Corten [8] explained this behavior by order magnitude analysis and argued that the pressure gradient balances the approximately uniform stream-wise Coriolis acceleration in the separated flow region.

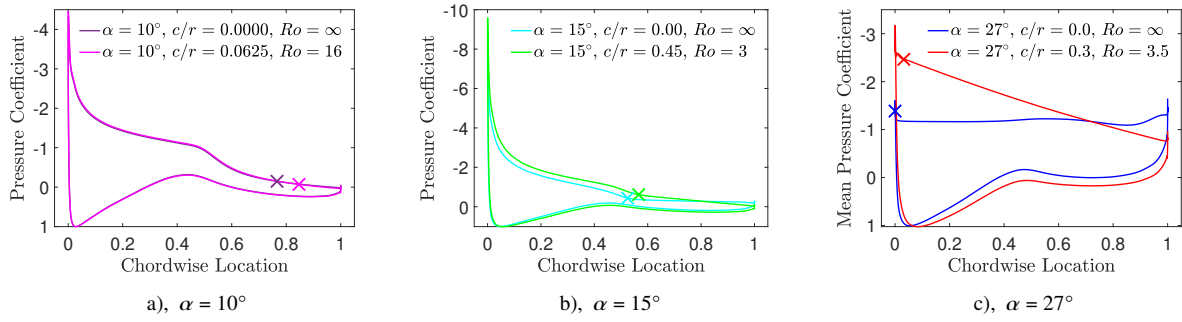


Fig. 6 Surface pressure distributions and upper surface separation points (markers) for the cases with and without rotation.

For the three angles of attack, it is seen that the pressure decreased throughout the upper surface as the c/r ratio increased and Ro decreased, i.e., as the rotational effect was enhanced. Furthermore, this offers an explanation for the irregular rotational effect on the drag. The increased suction on the aft portion of the airfoil contributed to increase the pressure drag, while the suction enhancement on the fore portion worked to reduce the pressure drag. The global effect was thus dictated by the balance between these two contributions [17].

The fields of velocity component in the span-wise direction along with streamlines for $\alpha = 10^\circ$, 15° and 27° considering the cases without and with rotation are shown in Fig. 7. It can be noticed that the radial velocity component was particularly strong in the separation region, given that there the velocity component parallel to the sectional plane was small. Hence, an unbalance between the centrifugal and radial component of Coriolis force turned the streamlines there towards the blade tip.

Moreover, from streamlines, we see that the rotation caused a significant reduction of the recirculation region's volume even for $\alpha = 10^\circ$, which considered a high value of Rossby number. As the model did not account for radial gradient of centrifugal force, this reduction cannot be attributed to drainage of span-wise vorticity through the centrifugal pumping. As pointed by Bangsa et al. [6], the volume reduction observed in the separated flow weakens the decambering effect associated with boundary layer's thickening on the suction surface, increasing the lift compared to the 2D condition. For $\alpha = 27^\circ$, the rotation caused a change of the time-averaged flow pattern as well. For 2D flow, two counter-rotating vortices occurred over the upper surface, whereas for the considered rotating condition, the counterclockwise vortex on the trailing edge was suppressed.

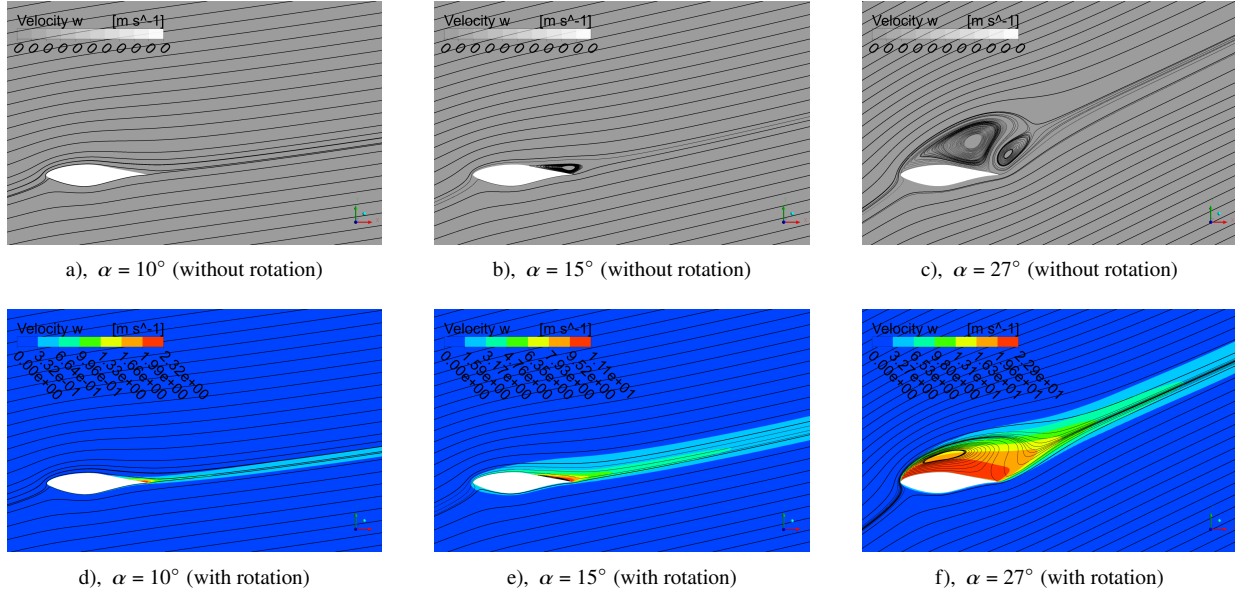


Fig. 7 Field of span-wise velocity along with streamlines for the cases without (top side) and with (bottom side) rotation considering $\alpha = 10^\circ, 15^\circ$ and 27° .

C. Effect of Coriolis acceleration

We investigated the effect of the Coriolis acceleration on the equilibrium of radial vorticity of the region of recirculating flow. In the radial-vorticity transport equation, the Coriolis acceleration's tangential component is associated to a term named by Werner et al. [12] as radial planetary vorticity tilting. Following the nomenclature used here, this term is given by

$$S_\omega = -2\Omega \left(\frac{\partial w}{\partial x} \sin \varphi + \frac{\partial w}{\partial y} \cos \varphi \right). \quad (5)$$

Contours of S_ω are shown in Fig. 8 together with the field of span-wise vorticity for $\alpha = 10^\circ, 15^\circ$ and 27° , respectively, with and without rotation. In general, it can be inferred that the upper-surface boundary layer fed the region of separated flow with span-wise vorticity of negative sign (in blue). For $\alpha = 10^\circ$, a low influence of rotational effects was observed, possibly due to the high Rossby number and low c/r adopted. Besides, the separated flow region, where stronger rotational effects are expected, was small. Figure 8 also shows a detailed view of the suction surface, which reveals a thin layer of positive-sign radial vorticity in all cases due to the reverse flow. The interaction of the clockwise rotating flow with this layer was suggested by Wojcik and Buchholtz [10] as a relevant mechanism for the stabilization of leading-edge vortex on insect wings.

In addition, we can see from Eq. (5) that S_ω is large in regions of intense gradient of w in the xy plane. Therefore, as shown in Fig. 8, high values of S_ω were observed in the upper limit of the separation region, which was a region of intense transport of negative vorticity into the recirculation region. Hence, S_ω may have destroyed part of the vorticity convecting from the mixing layer into the region of recirculating flow.

Based on the data of the cases with 15° AoA, we investigated the effect of S_ω on the velocity profile in the vicinity of the airfoil suction surface. Figure 9 illustrates the normal unit vectors calculated for several locations along the chord from a numerical method using a second-order centered finite difference scheme based on the airfoil coordinates [15]. Here we present results corresponding to selected locations on the upper airfoil surface.

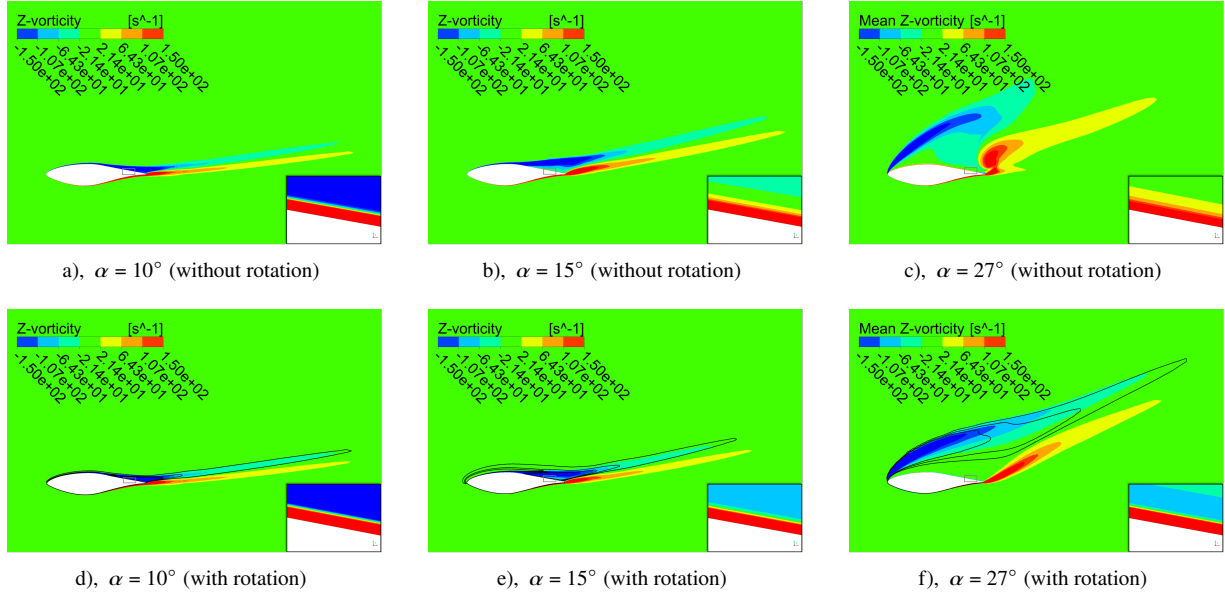


Fig. 8 Field of span-wise vorticity and detail of the vicinity of the upper surface along with contours of the term associated to the planetary vorticity tilting, S_ω , for the cases without (top side) and with (bottom side) rotation considering $\alpha = 10^\circ$, 15° and 27° . The values of the S_ω contours are $7s^{-2}$, $22s^{-2}$ and $37s^{-2}$ for $\alpha = 10^\circ$; $135s^{-2}$, $285s^{-2}$ and $435s^{-2}$ for $\alpha = 15^\circ$; $185s^{-2}$, $335s^{-2}$ and $485s^{-2}$ for $\alpha = 27^\circ$.

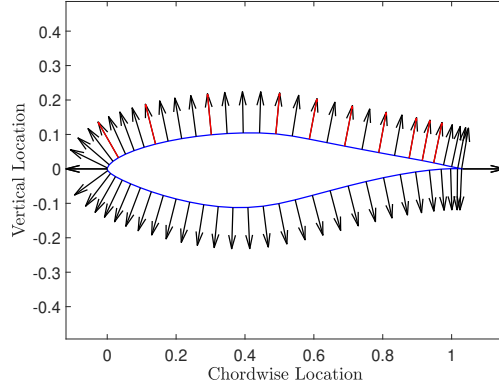


Fig. 9 Unit normal vectors calculated from a second-order centered finite difference scheme. The locations chosen for the next steps are highlighted in red.

Figure 10a) shows profiles of chord-wise and radial velocity components (u and w , respectively), S_ω and span-wise vorticity (ω_z) in a location of the attached boundary layer, namely at $x/c = 0.14$. The larger value of u outside the boundary layer for the case with rotation is consistent with the increased lift. It is worth noting that very negative values of S_ω were found confined in a very narrow region close to the airfoil wall. Nevertheless, no significant vorticity change was observed in the lower portion of the boundary layer due to rotation, as can be seen in Fig. 10b). We stress, however, that any observation regarding the boundary-layer region closest to the surface must be considered cautiously due to the substantial simplifications of the turbulence model in this region.

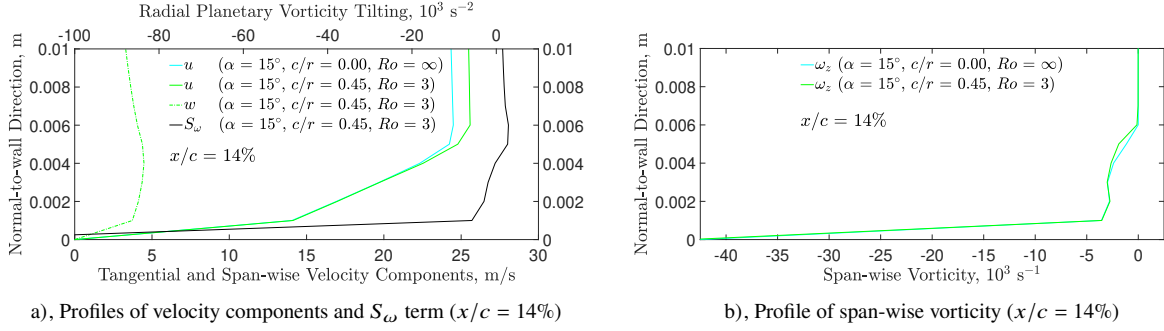


Fig. 10 Profiles of (a) chord-wise and radial velocity components and S_{ω} term and (b) span-wise vorticity along the local normal-to-wall direction for locations at $x/c = 14\%$ considering the cases with and without rotation.

Figure 11 shows the profiles for a location in the separated flow region at $x/c = 0.69$. Figure 11a) focus on the positive range of S_{ω} , but intense negative values were observed close to the surface. As expected from inspection of Eq. 5, high radial planetary vorticity tilting values were seen where gradients of w were significant. For instance, at the upper edge of the recirculation region, w decreased with the normal-to-wall distance. At this position, S_{ω} assumed its most positive value. It is worth noting that rotation did not significantly change the magnitude of the radial component of the local vorticity in the free shear layer, as can be seen in Fig. 11b). The span-wise vorticity profiles confirmed this observation at other locations, shown in Fig. 12. However, at locations further downstream in the region of recirculating flow, the integral of ω_z along the normal-to-wall direction reduced, as shown in Fig. 12b).

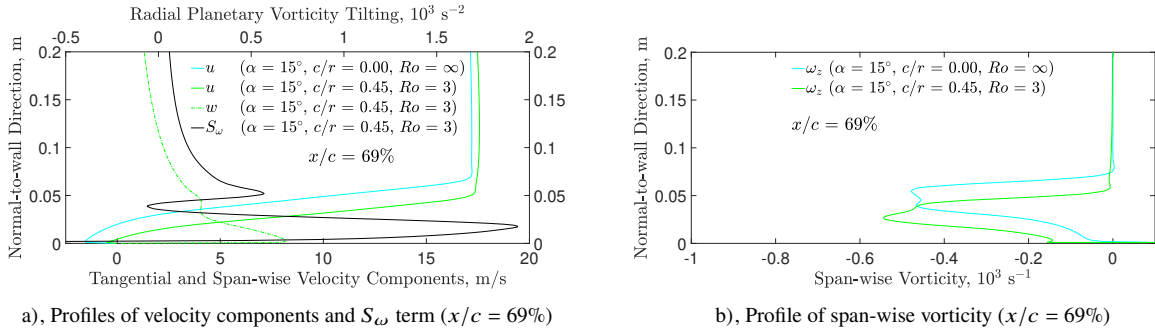


Fig. 11 Profiles of (a) chord-wise and radial velocity components and S_{ω} term and (b) span-wise vorticity along the local normal-to-wall direction for locations at $x/c = 69\%$ considering the cases with and without rotation.

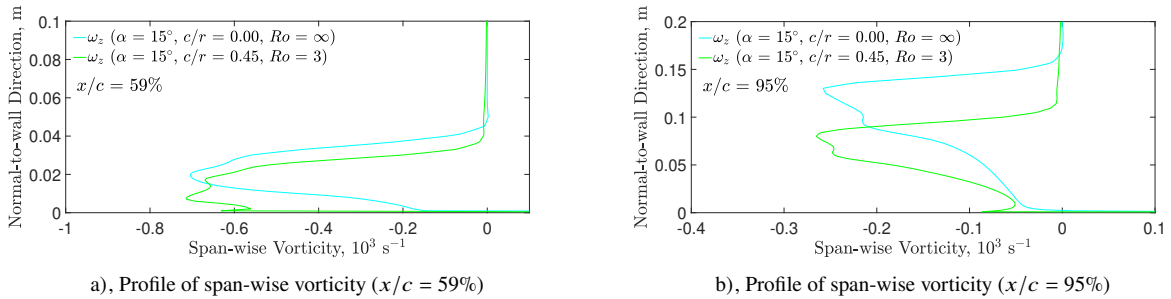


Fig. 12 Profile of span-wise vorticity along the local normal-to-wall direction for locations at $x/c = 59\%$ and 95% considering the cases with and without rotation.

The tangential component of the Coriolis force, which is responsible for pushing the flow towards the trailing edge, increases as w increases. As a result of the vertical gradient of w , there is a positive-sign torque in the fluid elements that opposes the span-wise vorticity of the boundary layer that flows into the recirculation region. This mechanism is known to stabilize the leading-edge vortex on fly wings [12, 20].

To evaluate the relevance of the destruction of vorticity through the radial tilting of the planetary vorticity, we integrated the term defined in Eq. (5) within a region containing the recirculating flow. The integration regions for the three cases with rotation are shown in Fig. 13. They were defined based on the contours of constant radial vorticity conveniently chosen to contain the recirculation. The integral of the Coriolis term was then compared to the flow rate of radial vorticity entering the integration region from the boundary layer through the blue line in Fig. 13.

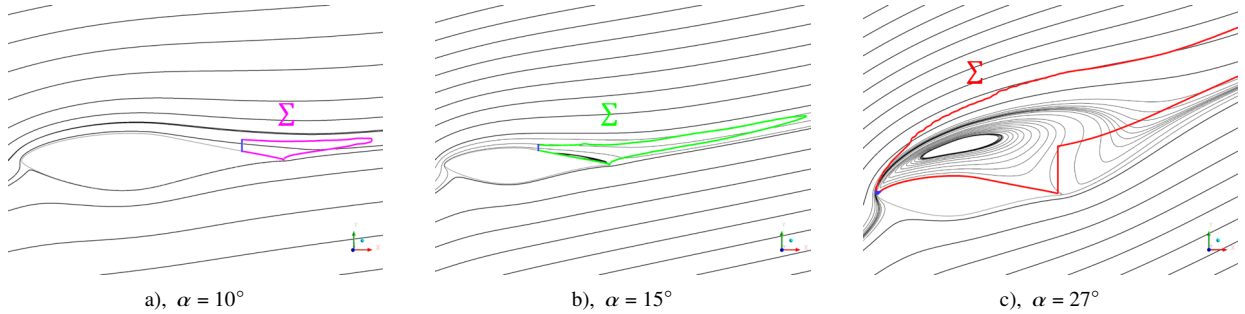


Fig. 13 Integration region of the Coriolis term of the radial vorticity equation. Limits based on the contour of radial vorticity equals to $-90s^{-1}$ for $\alpha = 10^\circ$, equals to $-30s^{-1}$ for $\alpha = 15^\circ$ and equals to $-1s^{-1}$ for $\alpha = 27^\circ$.

Table 2 presents the obtained ratio between the integral of S_ω and the radial-vorticity flow rate from the boundary layer V_{BL} for the cases with rotation and highlight the importance of the Coriolis effect to the balance of the radial vorticity within the region of separated flow. The value over 100% for the case at $\alpha = 27^\circ$, may be explained by the fact that the term associated with the curvature considered in the model is possibly transporting additional vorticity to the integration region, which may also be counteracted by the Coriolis effect.

Table 2 Ratio between the integral of S_ω and rate of radial vorticity flowing in from the boundary layer.

α	c/r	Ro	$\iint_{\Sigma} S_\omega d\Sigma / V_{BL}$
10°	0.0625	16.0	0.58%
15°	0.4500	3.0	21.92%
27°	0.3000	3.5	114.48%

IV. Conclusions

Quasi-3D simulations were performed to investigate the flow over sections of horizontal-axis wind turbines under rotation. The aim was to understand the role of the tangential component of the Coriolis acceleration on the balance of radial vorticity at high angles of attack. Simulations without rotation showed good correlations with 2D wind-tunnel experiments. Moreover, analyses were performed considering relevant conditions for blades of horizontal-axis wind turbines. The simulations captured the well-known effects of rotation on the flow. For the three considered angles of attack, the rotation significantly reduced the size of the region of recirculating flow. The rotation reduced the drag for the lowest angle of attack and increased it for the other two angles of attack, confirming previous results with span-wise-homogeneous simulations. Additionally, the gradient of the tangential component of the Coriolis force was shown to generate radial vorticity in the separation region of sign opposite to the vorticity advected from the upstream boundary layer. This mechanism was shown to destroy radial vorticity at a rate comparable to the rate flowing in from the boundary layer, which indicated that it might be relevant for the observed reduction of the separated flow region and thus for the rotational augmentation.

Acknowledgments

This research was supported by FAPESP under grants #2020/10972-3 and #2022/02812-1, São Paulo Research Foundation (FAPESP).

References

- [1] Dwyer, H., and McCroskey, W., “Crossflow and unsteady boundary-layer effects on rotating blades,” *Proceedings of 8th AIAA Aerospace Science Meeting*, New York, USA, 1970.
- [2] Ronsten, G., “Static pressure measurements on a rotating and a non-rotating 2.375 m wind turbine blade. Comparison with 2D calculations,” *Journal of Wind Engineering and Industrial Aerodynamics*, Vol. 39, 1992, pp. 105–118.
- [3] Dumitrescu, H., Cardos, V., and Dumitrache, A., “Modelling of inboard stall delay due to rotation,” *Journal of Physics: Conference Series*, Vol. 75, 2007.
- [4] Schreck, S., Soerensen, N., and Robinson, M., “Aerodynamic structures and processes in rotationally augmented flow fields,” *Wind Energy*, Vol. 10, 2007, pp. 159–178.
- [5] Mauro, S., Lanzafame, R., and Messina, M., “An insight into the rotational augmentation on HAWTs by means of CFD simulations - PART II: Post Processing and force analysis,” *International Journal of Applied Engineering Research*, Vol. 12, No. 21, 2017, pp. 10505–10529.
- [6] Bangga, G., Lutz, T., Jost, E., and Krämer, E., “CFD studies on rotational augmentation at the inboard sections of a 10MW wind turbine rotor,” *Journal of Renewable and Sustainable Energy*, Vol. 9, 2017, pp. 1–28.
- [7] Jardin, T., and David, L., “Spanwise gradients in flow speed help stabilize leading-edge vortices on revolving wings,” *Physical Review E*, Vol. 90, No. 1, 2014, pp. 312–340.
- [8] Corten, G., “Flow Separation on Wind Turbine Blades,” Utrecht, Netherlands, 2001.
- [9] Lindenburg, C., “Investigation into rotor blade aerodynamics,” Tech. rep., NOVEM, Netherlands, July 2003.
- [10] Wojcik, C., and Buchholtz, J., “Vorticity transport in the leading-edge vortex on a rotating blade,” *Journal of Fluid Mechanics*, Vol. 743, 2014, pp. 249–261.
- [11] Jardin, T., “Coriolis effect and the attachment of the leading edge vortex,” *Journal of Fluid Mechanics*, Vol. 820, 2017, pp. 312–340.
- [12] Werner, N., Chung, H., Wang, J., Liu, G., Cimbala, J., Dong, H., and Cheng, B., “Radial planetary vorticity tilting in the leading-edge vortex of revolving wings,” *Physics of Fluids*, Vol. 31, 2019, pp. 1–15.
- [13] Chaviaropoulos, P., and Hansen, M., “Investigating three-dimensional and rotational effects on wind turbine blades by means of quasi-3D Navier-Stokes solver,” *Journal of Fluids Engineering*, Vol. 122, 2000, pp. 330–336.
- [14] Menter, F. R., “Two-equation eddy-viscosity turbulence models for engineering applications,” *AIAA Journal*, Vol. 32, No. 8, 1994, pp. 1598–1605.
- [15] Somers, D. M., “Design and experimental results for the S809 airfoil,” Tech. rep., NREL, January 1997.
- [16] Herráez, I., Stoevesandt, B., and Peinke, J., “Insight into rotational effects on a wind turbine blade using Navier-Stokes Computations,” *Energies*, Vol. 7, 2014, pp. 6798–6822.
- [17] Souza, D., and Gennaro, E., “Rotational Effects on the Spanwise Periodic Flow over a Wind Turbine Airfoil,” *18th Brazilian Congress of Thermal Sciences and Engineering*, 2020, pp. 1–11.
- [18] Hand, M., D., S., Fingersh, L., Jager, D., Cotrell, S., J.R. Schreck, and Larwood, S., “Unsteady aerodynamics experiment phase VI: Wind tunnel test configuration and available data campaigns,” Tech. rep., NREL, Dezembro 2001.
- [19] Sicot, C., Devinant, P., Loyer, S., and Hureau, J., “Rotational and turbulence effect on a wind turbine blade. Investigation of the stall mechanisms,” *Journal of Wind Engineering and Industrial Aerodynamics*, Vol. 96, 2008, pp. 1320–1331.
- [20] Eldredge, J. D., and Jones, A. R., “Leading-edge vortices: mechanics and modeling,” *Annual Review of Fluid Mechanics*, Vol. 51, 2019, pp. 75–104.